Bulletin of the Seismological Society of America, Vol. 94, No. 1, pp. 357–362, February 2004

Site Response from Incident *Pnl* Waves

by Brian Savage and Don V. Helmberger

Abstract We developed a new method of determining site response and amplification for use in hazard analysis and station corrections. The method employs the conversion of *P* to *S* energy beneath a soft-rock station, which results in complex receiver functions that are frequency and amplitude dependent. At low frequencies (<0.1 Hz), the ratio of vertical to radial energies for *Pnl* appear uniform across the TriNet array, where shallow structures can be neglected. Ratios of high-frequency energies (>0.5 Hz) can be normalized to these low-frequency levels to quantify the amount of high-frequency amplification. Our results agree with previous studies of the Los Angeles Basin and provide the means of calibrating station responses at high frequencies.

Introduction

Characterization of how a seismic station responds to incident seismic waves, or site response, is important to many aspects of earthquake research. First, it describes which areas are prone to violent shaking during large earthquakes, or hazard assessment (Field, 2000). Second, knowledge of the velocity structure beneath a seismic station assists in station corrections used in tomography, waveform modeling studies, and earthquake location problems. Third, the velocity structure may be translated into tectonic structures at shallow to intermediate depths.

Site response is normally determined using receiver function analysis of either teleseismic *P* waves ($\Delta > 30°$) or short-period, local ($\Delta < 150$ km) *S* waves (Fig. 1). Both methods sample distinctly different portions of the crustal velocity structure. Teleseismic arrivals are relatively long-period *P* waves, (>1 sec) and are utilized in receiver function studies to determine crustal velocity profiles and thickness. At sharp interfaces, teleseismic *P* waves convert a portion of their energy into *S* waves, which appears on the radial component. These *P*-to-*S* conversions are well suited to crustal thickness studies or determining Moho depths (Langston, 1977). In contrast, teleseismic *P* waves do not perform well at determining shallow structure unless large velocity contrasts exist. Shallow velocity structures are well determined by local *S* waves. *S* waves cause the majority of damage during local earthquakes, and it is therefore appropriate to use local *S* waves to determine site response. Local *S* waves have frequencies from >0.5 Hz to in excess of 7 Hz. Frequencies of this range limit the sampling to the top few kilometers (Fig. 1). At very short distances, the window used to compute the site response contains the beginning portion of the surface wave. Surface waves are not solely representative of the local site response. Thus, the velocity structure between source and receiver becomes increasingly important. This effect is overcome by a sufficient number of events and stations within a region (Hough *et al.*, unpublished manuscript). Another complication with using local *S* waves is the need for a nearby reference station of known site response to calibrate the new response. This becomes important in the presence of basins or other complicated crustal structures (Hartzell *et al.*, 1998).

To compliment the use of teleseismic and local arrivals, we suggest the use of regional *P* waves (150 km $< \Delta <$ 1400 km). These arrivals are refractions along the crust–mantle interface, *Pn*, and the crustal *P* arrivals and *PmP* along with various *S* segments. For convenience we identify this set of arrivals as *Pnl* (Helmberger and Engen, 1980). Figure 1 shows the sampling region of *Pn*, *Pg*, and *PmP* from ray path and waveform perspectives. *Pnl* arrivals vary in frequency content from the longer period *Pn* (0.33 Hz) to the shorter period *Pg* and *PmP* arrivals (0.5–2 Hz). This frequency range allows *Pnl* to be used to determine larger scale local structures that are not easily accessible to local *S* or teleseismic arrivals. Figure 1 displays vertical- and radial-component displacement records from an earthquake on 8 December 2001 recorded by station LGB, which is situated within the Los Angeles Basin. Arrivals discussed previously are highlighted on the radial component as an example of their shape and timing from a waveform perspective.

Method

The angle of the wavefront, *i*, is affected only by the velocity of the medium, α, as the ray parameter, *p*, is constant in a simple layered structure:

$$p = \frac{\sin i}{\alpha}. \quad (1)$$

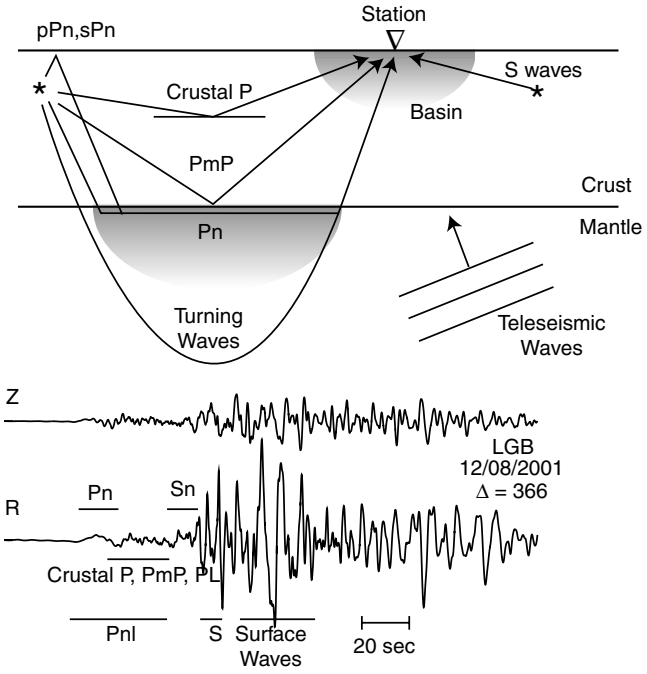

Figure 1. Cartoon of sampling and ray paths of many arrivals present in local and regional recordings of earthquakes, $\Delta < 14°$. A teleseismic wave field is also included. The inverted triangle is a seismic station located on top of a basin, shaded in gray near the surface. The stars are earthquake sources. The shaded region directly below the crust–mantle interface indicates the sampling region of the *Pn* wave field in the mantle. Below the cartoon are vertical and radial displacement data from an earthquake in southern California on 8 December 2001 recorded at station LGB (Laguna Bell). Portions of the waveform are highlighted for reference. The data are displayed on the same vertical scale.

As a wavefront encounters slower velocities, its direction becomes increasingly vertical when arriving at a station. Figure 2 shows the waveform differences between two velocity models. The first model emulates a hard-rock station (V_p = 5 km/sec; 2 km deep), while the second is similar to a soft-rock station (V_p = 2 km/sec; 2 km deep). The crust–mantle interface for both models is set at 35 km, the source-receiver distance is 175 km, and the source depth is set at 17 km. This geometry makes *Pn* the first arrival at slightly further than critical distance. All waveforms on each row are plotted on the same amplitude scale. Moreover, the top three rows are on the same amplitude scale. Displacement generalized ray responses (Helmberger, 1983) were computed for *Pn* + *PmP* arrivals and the *P*-to-*S* conversion response near the surface, shown in the first two rows. These responses are then summed and filtered to produce the waveforms in the fourth row. When the ray path becomes vertical, an increasingly larger proportion of energy will appear on the vertical component, as *P* is polarized along the propagation direction. This effect is opposite for *S* waves, where the polarization is perpendicular to the propagation direction. As the *S* wave encounters slower velocities, it turns vertical and the energy appears on the radial component. This effect is shown in the waveforms and in the polarization-angle graphs between the second and third rows. Recent studies used the polarization of *S* waves as a theoretical basis to do single-station estimates of site amplification (Nakamura, 1989; Lermo and Chavezgarcia, 1993; Siddiqqi and Atkinson, 2002).

Similar to teleseismic arrivals, *Pnl* arrivals convert *P* energy to *S* energy at interfaces. Larger contrasts amplify the conversion, resulting in larger *S* arrivals. Synthetics for the soft-rock model in Figure 2 show this. Converted *P* to *S* energy, as with local *S* waves, appears on the horizontal component. The combination of arriving *P* and *S* energy on the radial component results in an apparent longer period arrival when compared to the same arrivals on the vertical component. The radial component appears longer period as the *S* wave has opposite polarities on the vertical and radial components, in addition to the substantial *S*-wave amplification occurring from large velocity contrasts. When these arrivals are filtered, either by a low-pass filter or source effect, the apparent period of the radial component increases relative to the vertical component.

The bottom row of seismograms in Figure 2 displays data from a hard-rock and a soft-rock station. The amplitude and shape of the hard-rock vertical and radial components are similar, indicating the *Pnl* arrival is arriving as a coherent wave packet. In contrast, the soft-rock components show differences between the radial and vertical components. The radial component decreases in amplitude and becomes longer period, while the vertical component is larger in amplitude and shorter period. This waveform behavior will be exploited to determine the amplification at a specific site.

Using the propagation effects highlighted in Figure 2 as a basis, we employ a vertical-to-radial energy ratio to determine the amplification of incident, extended *P* waves at a broadband station. We use a record duration around the *Pn* arrival of 10 sec before, t_0, and about 35 sec after, t_1. We assume the initial portion of the *Pnl* arrival travels with a velocity of 7.8 km/sec, which is average for southern California (Hadley and Kanamori, 1977) and many parts of the world. From this velocity and the source-receiver distance, a *Pnl* onset time is calculated and used as the reference time. Use of this time window limits the arriving energy to be compressional (*P*) and associated *S* conversions near the receiver, rather the heavily *S*-dominated energy later in the *Pnl* arrival. We then take a ratio of the vertical to radial energy to determine the amplification:

$$A = E^{1/2} = \left(\left[\frac{\int_{t_0}^{t_1} [v_z^2]_{\omega_1}}{\int_{t_0}^{t_1} [v_z^2]_{\omega_2}} \right] \Big/ \left[\frac{\int_{t_0}^{t_1} [v_r^2]_{\omega_1}}{\int_{t_0}^{t_1} [v_r^2]_{\omega_2}} \right] \right)^{1/2}. \quad (2)$$

The vertical and radial velocity components are v_z and v_r, respectively. We square each waveform within the window specified earlier, then integrate to obtain the energy for each

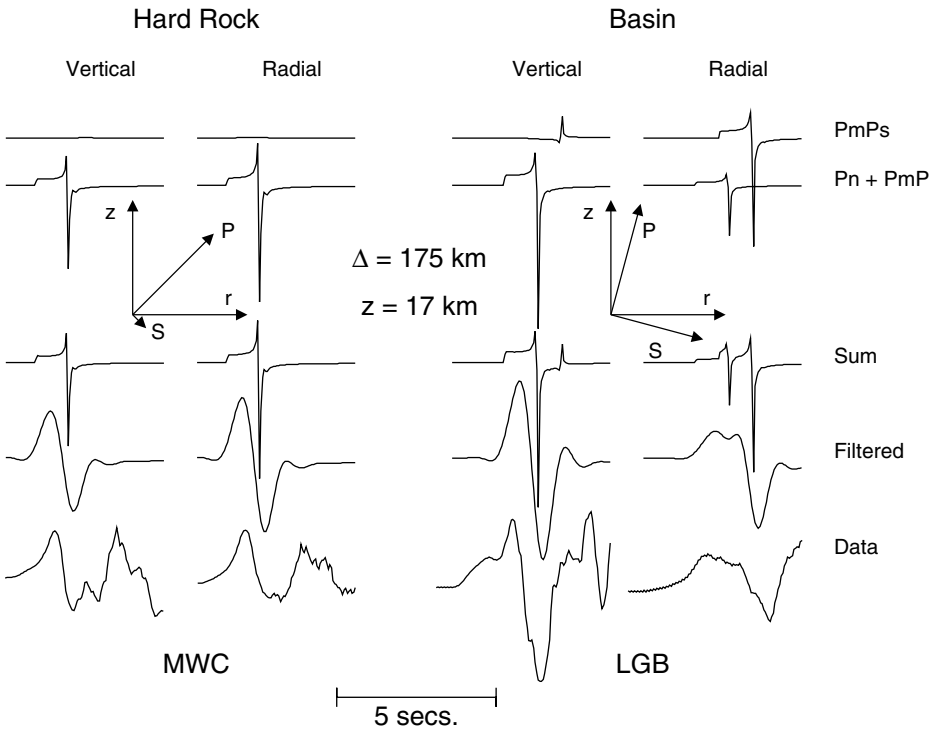

Figure 2. Comparison of seismograms from two different types of upper crustal velocity models. The two left-hand columns are created from a hard-rock-type model and show the vertical and radial component. The right two columns are the vertical and radial components for a soft-rock-type model. The individual generalized ray responses in the top two rows are summed in the third row, then filtered in the fourth row. Each seismogram is made up of a single Moho reflection plus the *P*-to-*S* conversion at a 2-km-deep boundary. Hard-rock seismograms look similar on the vertical and radial components. In contrast, soft-rock seismograms have different shapes due to the increased vertical ray paths and the *P*-to-*S*-wave conversion at depth. The *P*-to-*S*-wave conversion widens the arrival on the radial component. The crust–mantle interface is set at 35 km depth, the source, *z*, is at 17 km, and the source-receiver distance is 175 km.

record. This procedure is carried out for a variety of different frequencies. We use a low-pass, a-causal, Butterworth filter at a range of various frequencies. By dividing the higher frequency energy, ω_1, by one at a lower frequency, ω_2, we obtain the amount of energy arriving within a specific period band. Division of the vertical component by the radial component removes any source and propagation effects. Amplification of *Pnl* arrivals occur on the vertical component as the ray direction turns more vertical upon encountering slower velocities near the station. We do not use a reference station, but rather assume that the reference amplification is around 1. This is shown later to be a safe assumption, as the minimum value obtained from full waveform synthetics and data waveforms is approximately 1 for hard-rock models.

Figure 3 displays displacement data and two energy ratios versus time (*V*/*R* and *R*/*V*). We have set the lower frequency to be 0.1 Hz and the higher frequency to be 3 Hz. Concerning the first ratio (*V*/*R*) at station MWC, a hard-rock site, the energy ratio stays near 1. This is in contrast to station LGB, a soft-rock site, whose energy ratio becomes almost 30. As the time enters the *Pnl* regime, the energy ratio grows governed by the phenomena highlighted in Figure 2. Leaving the *Pnl* regime and encountering the *S* wave and surface wave, the energy ratio drops. This decrease is due to large amounts of arriving horizontal energy. Therefore the energy ratio measure is sensitive to the choice of integral duration, t_0 to t_1. We suggest taking the maximum value of the measure constrained within the *Pnl* regime; however, using a set window length will only affect results if the duration is too long. The opposite effect is apparent for the second energy ratio (*R*/*V*). The ratio is nearly 1 through the arrival of *Pnl*. When the *S* waves begin to arrive, the ratio of radial to vertical, as proposed by Nakamura (1989), increases until reaching a stable value during the surface waves. Moreover, a comparison of this ratio at MWC and LGB shows a pronounced amplification at the soft-rock station LGB.

To test this, we calculated frequency-wavenumber synthetics for a range of velocities ($\pm 15\%$) and layer thicknesses (± 3 km) of the top layer. These synthetics are computed from a flat-layered model with the same velocity structure at the source and receiver. Taking a ratio of energies allows the removal of source side effects negating the

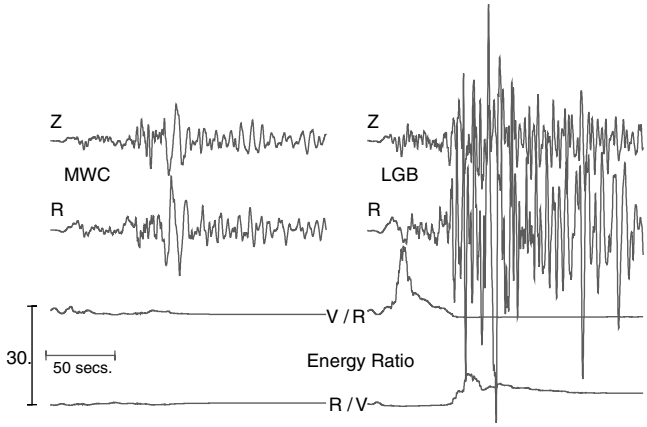

Figure 3. Effect of window duration, t_0 to t_1, on energy ratio. The top two rows are vertical and radial displacement records for stations MWC (Mount Wilson) and LGB (Laguna Bell). All records are on the same vertical scale. The bottom two rows show the energy ratio (*V*/*R*) and its inverse (*R*/*V*). As the measure leaves the *Pnl* regime and enters the *S*- and surface-wave regime, the first ratio descends toward 1 while the second increases due to the large amount of arriving horizontal energy. The lower frequency employed here is 0.1 Hz, and the higher frequency is 3.0 Hz. These energy ratios assume an initial starting time of t_0 before the first arrival, and the value of the energy ratio for any particular t_1 is the value shown at that particular time, that is, no integration is necessary.

one-dimensionality of our model. Our synthetic model is equivalent to the amplification at the middle of a large basin with flat, homogeneous layers. The synthetic model setup places both source and receiver within the slow velocities, similar to the middle of a very large basin. We expect increased amplification near basin edges due to a focusing effect (Scrivner and Helmberger, 1994). As the velocities of the layer become slower, the amplification of *Pnl* increases. The maximum amplification we see for the window length defined in equation (2) is 3.9, with the minimum near 1. The correlation of amplification with layer thickness is not as strong as with velocity, especially at higher frequencies.

Data and Analysis

To compute amplification factors for southern California, we employed broadband velocity records recorded by TriNet. These records have flat and stable instrument responses in the frequency range of interest. The instrument responses are removed as not to bias one station to another. Using only the regional records greater than 175 km allows us to capture only the *Pnl* arrival. Amplitude ratios, or the square root of the energy ratios, are computed for an event (8 December 2001, northern Mexico, M_w 5.8) and plotted in Figure 4 for all of southern California (top panel) and centered on the Los Angeles Basin region (lower panels). The lower left-hand panel of Figure 4 displays the topography and the measured amplitude ratios at individual broadband stations. On the lower right of Figure 4 is the interpolation of the amplitude ratio data. The results for this event agree well with other amplification studies (Hartzell *et al.*, 1998; Hough *et al.*, unpublished manuscript). Note that the largest amplifications appear in the regions with the deepest basins. However, larger-than-expected amplification factors are seen to the northwest and southeast of the deepest portion of the basin, below stations USC, OLI, and BRE. These areas are influenced by the basin edge. While this is not a true representation of amplification from a 1D velocity structure, it does show the variability that may occur from regional earthquakes. This effect is similar to to surface-wave contamination of local *S*-wave estimates of amplification. However, computation of finite difference synthetics also shows increased amplification near the edges of basins (i.e., Scrivner and Helmberger, 1994).

We have not calibrated our amplification factors against those derived from local *S* waves due to the large number of source-receiver pairs required. It does appear, however, that amplifications from this study do agree well in spatial pattern and reasonably in absolute magnitude. It is further encouraging that our minimum is near 1 and our maximum amplification is near the local *S*-wave maximum, both similar to our synthetic model mentioned previously.

Conclusions

Through the use of a *Pnl* ratio of vertical to radial energy, we are able to quantify the effects of site response. An amplification factor is computed that is similar to local, high-frequency *S* waves. In contrast to *S* waves, the *Pnl* ratio senses deeper into the crust. This method is particularly suited for discriminating the edges of large basins, which can be hazardous during medium to large earthquakes. Further work is necessary to determine if basin structures can be mapped through these methods. This method can be used in conjunction with local *S* waves and teleseismic *P* waves to further constrain site response.

Acknowledgments

This research was supported by the U.S. Geological Survey under Grant Number 02HQGR0063. The authors would like to thank Hiroo Kanamori for helpful discussions. This is Contribution Number 8954, Division of Geological and Planetary Sciences, California Institute of Technology.

References

Field, E. (2000). Accounting for site effects in probabilistic seismic hazard analyses of southern California: overview of the SCEC phase III report, *Bull. Seism. Soc. Am.* **90,** S1–S31.

Hadley, D., and H. Kanamori (1977). Seismic structure of Transverse Ranges, California, *Geol. Soc. Am. Bull.* **88,** 1469–1478.

Hartzell, S., S. Harmsen, A. Frankel, D. Carver, E. Cranswick, M. Meremonte, and J. Michael (1998). First-generation site-response maps for the Los Angeles region based on earthquake ground motions, *Bull. Seism. Soc. Am.* **88,** 463–472.

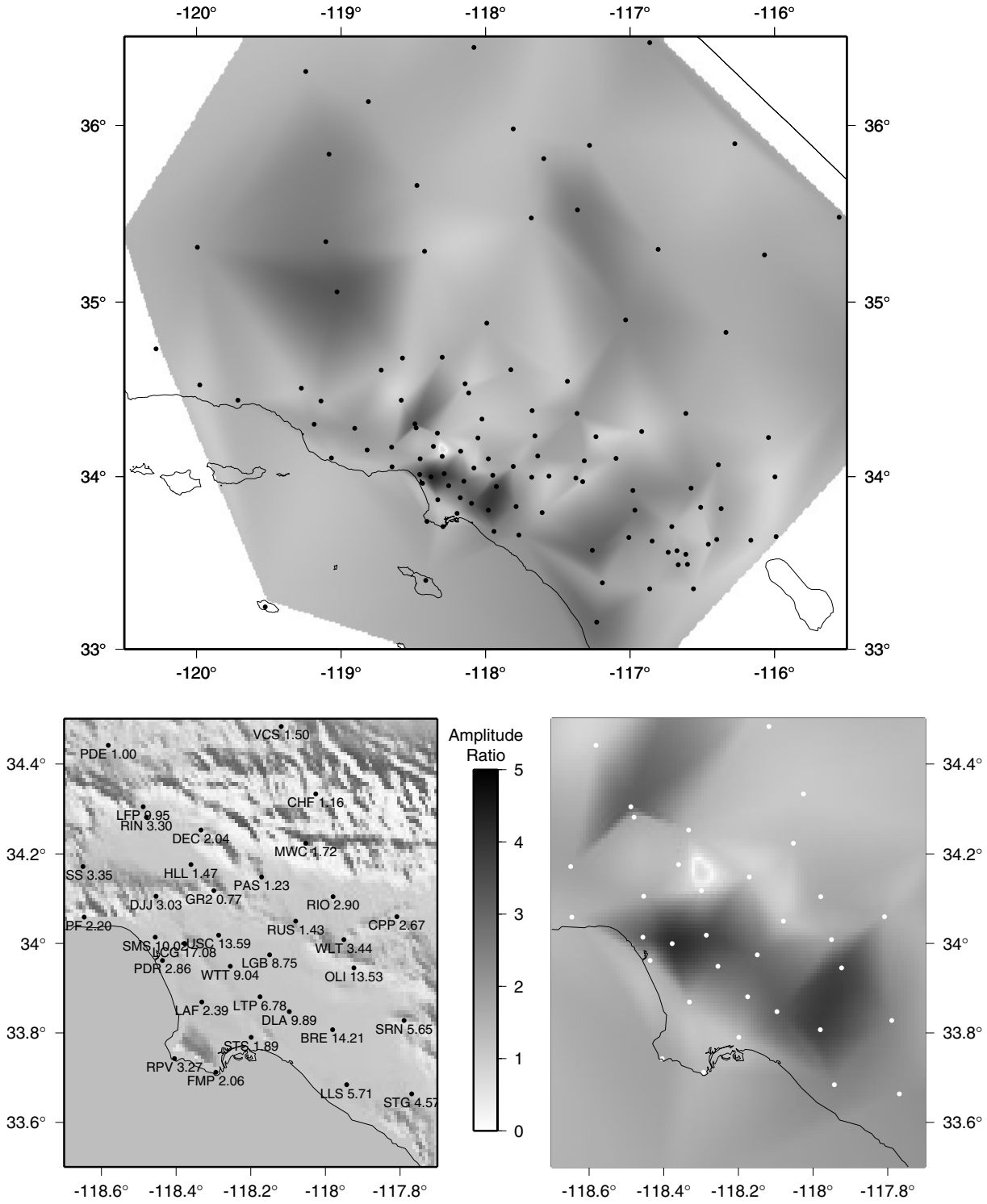

Figure 4. Map of amplification factors for southern California and the Los Angeles Basin region using a low frequency of 0.1 Hz, a high frequency of 3.0 Hz, a t_0 of 10 sec before *Pnl* (7.8 km/sec), and a t_1 of 35 sec following. The left-hand panel shows topography and amplification factors. The right-hand panel shows the interpolated grid using the data in the left-hand panel. Areas to the northwest and southeast show increased amplification when compared to the center of the Los Angeles Basin due to basin edge effects (Scrivner and Helmberger, 1994). Points represent broadband seismic stations, with names and amplifications following. The darker the shading, the larger the amplification.

Helmberger, D. (1983). Theory and application of synthetics seismograms, in *Earthqaukes: Observation, Theory, and Interpretation*, H. Kanamori and E. Boschi (Editors), North-Holland, Amsterdam, 174–222.

Helmberger, D. V., and G. R. Engen (1980). Modeling the long-period body waves from shallow earthquakes at regional ranges, *Bull. Seism. Soc. Am.* **70,** 1699–1714.

Langston, C. (1977). Corvallis, Oregon, crustal and upper mantle receiver structure from teleseismic *P* waves and *S* waves, *Bull. Seism. Soc. Am.* **67,** 713–724.

Lermo, J., and F. Chavezgarcia (1993). Site effect evaluation using spectral ratios with only one station, *Bull. Seism. Soc. Am.* **83,** 1574–1594.

Nakamura, Y. (1989). A method for dynamic characteristics estimation of subsurface using microtremor on the ground surface, *Quarterly Report Railway Technical Research Institute* **30,** 25–33.

Scrivner, C., and D. Helmberger (1994). Seismic wave-form modeling in the Los-Angeles basin, *Bull. Seism. Soc. Am.* **84,** 1310–1326.

Siddiqqi, J., and G. Atkinson (2002). Ground-motion amplification at rock sites across Canada as determined from the horizontal-to-vertical component ratio, *Bull. Seism. Soc. Am.* **92,** 877–884.

Seismological Laboratory
Division of Geological and Planetary Sciences
Mail Code 252-21
California Institute of Technology
Pasadena, California 91125

Manuscript received 22 July 2003.